Inhomogeneity scale lengths in a magnetized, low-temperature, collisionless, Q-machine plasma column containing perpendicular-velocity shear

E. W. Reynolds[a] and M. E. Koepke
Department of Physics, West Virginia University, Morgantown, West Virginia 26505-6315

J. J. Carroll
Department of Physics and Astronomy, Eastern Michigan University, Ypsilanti, Michigan 48197

S. Shinohara
Interdisciplinary Graduate School of Engineering Sciences, Kyushu University, Kasuga, Fukuoka 816-8580, Japan

(Received 20 September 2005; accepted 28 July 2006; published online 11 September 2006)

Radial inhomogeneity scale lengths for radial electric field, ion density, and magnetic-field-aligned (parallel) electron-drift velocity have been measured and interpreted in magnetized, low-temperature, collisionless plasma. The effect of a narrow layer of inhomogeneity in these parameters on the excitation of electrostatic ion-cyclotron waves is investigated. When the ion Larmor radius ρ_i is on the order of, or larger than, the half-width at half-maximum $\sigma_r\{E_r\}$ of the Gaussian-like, radially localized, radial electric-field profile $E_r(r)$, the radial profile of the azimuthal ion rotation velocity, measured using laser-induced fluorescence (LIF), has a peak that, because of finite-Larmor-radius effects, is significantly lower than the peak of the combined radial profile of the $\mathbf{E}\times\mathbf{B}$ and diamagnetic drift velocities. Results of an experimentally validated test-particle simulation are presented and applied using experimentally relevant electric-field profiles. Two experimental configurations are explored for which the ions enter into the electric field at different rates. In one configuration, the ions experience an effectively adiabatic increase in electric-field strength. In the other configuration, the increase in electric-field strength is effectively instantaneous. The simulation reproduces both the main features of the radial profile of LIF-measured ion flow and the observed density depletion in regions of relatively high plasma potential for experimental conditions in which no waves were observed. The density depletion is interpreted as resulting from the finite-Larmor-radius ion orbits in the presence of an inhomogeneous electric field with radial scale length $\sigma_r\{E_r\}\approx\rho_i$. © *2006 American Institute of Physics*. [DOI: 10.1063/1.2338293]

I. INTRODUCTION

A variety of free-energy sources able to excite coherent plasma waves are available in the real-world plasmas found in the laboratory and space. Many of these free-energy sources are associated with inhomogeneity present in the plasma system. The simplest interpretation of plasma stability in such an inhomogeneous system is based on coordinate-specific (i.e., local) values of the growth rate calculated using the local values of the plasma conditions. In some cases, this approach gives the wrong answer, one example being when the scale size of the inhomogeneity responsible for ion waves is smaller than an ion gyroradius. The quenching of current-driven electrostatic ion-cyclotron (CDEIC) waves due to the finite-diameter of the current channel responsible for the excitation of the instability is called "filamental quenching."[1] Cartier *et al.*[2] demonstrated that CDEIC waves become filamentally quenched when the ratio of the ion gyroradius ρ_i to the half-width at half-maximum of the current-channel diameter $\sigma_r\{v_d\}$ increases to unity. As $\rho_i/\sigma_r\{v_d\}$ becomes close to or greater than unity, the ions spend a significant part of their orbit outside the current channel. The analogous process involving the inhomogeneous energy-density driven instability[3] (IEDDI) would be the shrinking of the radial scale size $\sigma_r\{E_r\}$ (half-width at half-maximum) of the inhomogeneous radial electric field to the value of the ion gyroradius. As $\rho_i/\sigma_r\{E_r\}$ becomes close to or greater than unity, the ions no longer drift with the electrons at the $\mathbf{E}\times\mathbf{B}$ velocity. Such narrow electric-field layers will create favorable conditions for the electron-ion hybrid instability[4–10] if the $\mathbf{E}\times\mathbf{B}$ flow of the electrons is sufficiently large. Issues of scale length and nonlocal modes of plasma instabilities are relevant to numerous space-plasma processes.[11]

Perpendicular-velocity shear can be produced by introducing radial inhomogeneity of the radial electric field, thus causing inhomogeneity in the $\mathbf{E}\times\mathbf{B}$ drift-velocity profile for electrons and ions. In Q-machines,[12] such electric fields have been produced using biased, radially segmented, circular-electrode segments. A range of scale lengths, associated with the radial scale length of the radial electric-field profile, have been observed in space and laboratory plasma.[13] However, attention to the role played by an inhomogeneous electric-field profile in determining the actual radial profile of ion

[a]Electronic mail: plasmaeric@yahoo.com

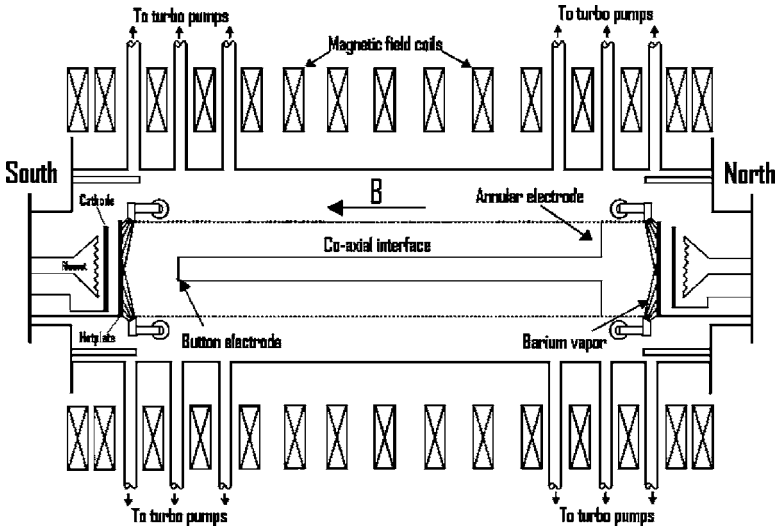

FIG. 1. Schematic view of the double-ended Q-machine showing the disk and annular electrodes (each located 40 cm from the respective source). The LIF diagnostic is located 25 cm from the disk electrode, while the emissive and Langmuir probes are located 60 cm from the disk electrode.

flow and ion density has been inadequate. Note that for IEDDI, it is the inhomogeneous perpendicular ion-drift profile, not the perpendicular electron-drift profile, that provides the free energy for growth. Therefore, if the perpendicular ion-drift profile is different from the electric-field profile, the pertinent inhomogeneity may be misinterpreted. The maximum values of $\rho_i/\ell_r\{n_i\}$ and $\rho_i/\sigma_r\{E_r\}$ measured in the present experiment are 2.2 and 4.6, respectively, where the density-gradient's inhomogeneity scale length $\ell_r\{n_i\}$ is defined as $1/\ell_r\{n_i\}\equiv[1/n_i(r)dn_i(r)/dr]_{\max}\equiv 1/[L_n(r)]_{\min}$ and $L_n(r)$ is defined as the density-gradient scale length.

The equilibrium velocity-distribution function for plasma with an inhomogeneous electric-field profile was first obtained analytically by Ganguli *et al.*[3] for $\rho_i/\sigma_r\{E_r\}\ll 1$ and uniform plasma density. It was shown that for small $\rho_i/\sigma_r\{E_r\}$, the ions drift with the full $\mathbf{E}\times\mathbf{B}$ velocity but with a change in the effective ion temperature, evaluated in the direction of $\mathbf{E}\times\mathbf{B}$ flow, which depends upon the magnitude of the velocity shear relative to the local ion-cyclotron frequency [as expressed later in Eq. (3)]. The stability of this equilibrium and the evolution of the unstable equilibrium were tested in particle-in-cell simulations[14–16] (for $\rho_i/\sigma_r\{E_r\}$ as large as unity), where it was shown that the ion-flow profile could relax significantly due to reduction of the perpendicular electric-field magnitude by nonlinear wave effects. The Vlasov equation was solved numerically by Cai *et al.*[17] for arbitrary values of shear in both linear and hyperbolic-tangent electric-field profiles. However, these works do not address the problem of how the equilibrium ion-flow profile develops. The present paper addresses the case of a Gaussian electric-field profile for arbitrary values of $\rho_i/\sigma_r\{E_r\}$ using a test-particle simulation that, for a hyperbolic-tangent electric-field profile, reproduces the results of Cai *et al.*[17] The Gaussian shape is used because it fits our measured electric-field profile better than the hyperbolic-secant-squared profile used by Ganguli *et al.*[3] Using our simulation, we analyze different methods of introducing ions into the electric-field structure and show that the resulting equilibrium ion drift and temperature is sensitive to the rate at which the ions enter the electric-field structure. Polarization electric fields are neglected in the test-particle simulation due to the experimental observation that these fields are overcome by the abundant supply of electrons from the hot plates and the constant voltage difference maintained by externally applied voltage between the plasma boundaries (i.e., electrodes and/or hot plates).

Section II describes our experimental arrangement, the production of collisionless, magnetized plasma, and the diagnostics used to characterize the resulting equilibrium. In Sec. III, the radial inhomogeneity parameters, $\sigma_r\{E_r\}$, $\ell_r\{n_i\}$, and $\sigma_r\{v_d\}$, of the radial electric field, ion density, and current channel, respectively, are measured and compared to a model in order to understand the ion dynamics associated with these inhomogeneity scale lengths in the West Virginia University Q-Machine[18] (WVUQ). The influence of the inhomogeneity parameters on measured ion-cyclotron mode characteristics is documented. The effect of large $\rho_i/\sigma_r\{E_r\}$ on the radial profile of both ion density n_i and azimuthal ion drift V_θ is demonstrated. Here, $\rho_i/\sigma_r\{E_r\}$ ($\rho_i/\ell_r\{n_i\}$) has been varied from 0.4 (0.15) to 2.9 (1.3), using sodium plasma and from 0.8 (0.45) to 4.6 (2.2) using barium plasma. For the case of barium plasma, V_y is measured by laser-induced fluorescence[19] (LIF) and compared with $\mathbf{E}\times\mathbf{B}$ drift $V_{\mathbf{E}\times\mathbf{B}}$ and ion diamagnetic drift $V_{\nabla p}$ velocities as inferred from the measured radial profiles of plasma potential and ion density using a fluid, slab geometry model [i.e., $(V_{\mathbf{E}\times\mathbf{B}})_y=-E_x/B_z$ and $\mathbf{V}_{\nabla p}=(\nabla p\times\mathbf{B})/(qn_iB^2)$]. Note that V_y is measured as a function of x at $y=0$ such that $V_y(x)=V_\theta(r)$. The discrepancy between the measured and inferred profiles of V_y is addressed in Sec. IV by a test-particle simulation that reproduces the main features of the observed ion-flow profile. The results can be found in Sec. V.

II. EXPERIMENTAL SETUP

Figure 1 shows a schematic view of the WVU Q-machine (WVUQ). WVUQ has two plasma sources, each of which is located at opposite ends of a 3-m-long plasma column. The 4-m-long chamber is centered in a set of solenoidal magnetic-field coils that produce a homogeneous

magnetic field up to 0.31 T. Each plasma source consists of a heated, 6.4-cm-outer-diameter, tungsten disk (hot plate) and an alkali-metal-vapor source (oven). The hot plates are heated to 2000 K by electron bombardment[20] (from outboard electron sources) and plasma is produced by contact ionization of alkali metal vapor on the inboard (i.e., front) surface of the hot plate. The front surface is coated with rhenium to increase the ionization probability.[21] Each hot plate can be independently biased. Simultaneous operation of the two sources results in two separate ion populations.

For the experiments presented here, WVUQ is operated in two different configurations. In one configuration, illustrated in Fig. 1, both plasma sources (at $z=0$ cm and $z=300$ cm) are simultaneously producing ions and electrons. An electrically floating annular electrode with 6.4-cm outer diameter and 2.5-cm inner diameter is located at $z=40$ cm while a biasable, 2.5-cm-outer-diameter disk electrode is located at $z=260$ cm. This configuration is referred to as DIDE[22] (double ionizer, double electrode) and results in coaxial, counter-streaming plasma populations for all axial positions between the electrodes. The two plasma populations are radially separated by a magnetically mapped boundary at $r=1.25$ cm, corresponding to the interface between the disk and annular electrodes. Application of a differential bias between the two hot plates results in a difference in plasma potential between the coaxial plasma populations and a corresponding radial electric field just inside ($r\approx 1.0$ cm) the coaxial interface at $r=1.25$ cm. The difference in the plasma potential of the two coaxial plasma populations is equal to the differential bias applied between the hot plates. This means polarization electric fields are overcome by the constant voltage difference maintained between the two hot plates in the DIDE configuration.

For the other configuration, only one plasma source is operated (at $z=0$) and a segmented-disk electrode[23] is positioned at $z=200$ cm. The segmented electrode consists of an 8-mm-diameter disk centered in an annular electrode with 1-cm inner diameter and 2.0-cm outer diameter. Each segment of the electrode is independently biasable. Application of a positive bias to a segment results in a flow of electrons along the magnetic-field lines intersecting that segment and a corresponding increase in plasma potential on those magnetic-field lines. Thus, control over the magnitude of radial electric fields generated at the edge of the electrode segments can be obtained by applying a bias to the corresponding segments. This same-end plasma-production method of generating inhomogeneous radial electric fields at the interface of coaxial plasmas has a limited range of experimentally realizable electric-field strengths compared to the previously described DIDE method. The typical plasma parameters are the plasma density n, which is on the order of 10^{15} m^{-3}, and electron and ion temperatures (T_e and T_i, respectively), which are 0.2 eV unless otherwise specified.

The two configurations described here illustrate an important difference in the rate at which ions are introduced into the electric-field structure. In the DIDE configuration, the ions pass by the disk electrode or annular electrode, depending which source they come from, into the axial region containing the electric-field structure in a fraction of an ion-cyclotron period. Ions that enter the electric-field structure encounter an effectively nonadiabatic increase in electric-field strength. For the other configuration, the electric-field strength increases smoothly from zero at the hot-plate surface to some nonzero value beyond the hot-plate sheath. When this happens over many cyclotron periods, it represents an effectively adiabatic increase in electric-field strength. It will be shown that ions experience an increase in radial oscillatory velocity, for instantaneous onset of the electric field, that becomes smaller as the increase in electric-field strength becomes more adiabatic. According to this interpretation, the DIDE configuration would be characterized by an elevated ion temperature perpendicular to the magnetic field. Measurements using LIF reveal that the ion temperature perpendicular to the magnetic field is indeed elevated in the DIDE configuration, giving us confidence in the above interpretation.

III. EXPERIMENTAL RESULTS AND DISCUSSION

A. Radial profile of magnetic-field-aligned current

Drummond and Rosenbluth[24] explained the excitation of CDEIC waves[25] using a model with a homogeneous electron drift parallel to the ambient magnetic field. However, past experiments on CDEIC waves[26] have found that a finite-diameter current channel with ρ_i an order-of-magnitude smaller than $\sigma_r\{v_d\}$ is sufficiently homogeneous for the experimentally determined threshold value of electron-drift velocity to agree with the predicted value from this theory. In experiments performed in WVUQ, a localized radial electric field is generated within this current channel and varied independently from the radial electric field at the channel boundary. Thus, the effect of the channel-internal electric field is isolated from the effect of the channel-boundary electric field.

The radial profile of the magnetic-field-aligned (i.e., parallel) drift of electrons with respect to the ions within the current channel created by the segmented-disk electrode is measured with a radially inserted, single-sided probe. The full width at half-maximum of the current channel is primarily determined by the magnetic mapping of the segmented-disk electrode along the plasma column. By varying the magnetic-field strength and the ion species, the relative size of the current channel with respect to the ion gyroradius can be adjusted. The instability mechanism responsible for the onset of CDEIC waves is the free energy associated with the electron drift relative to the ions. The threshold electron-drift velocity necessary for the onset of CDEIC waves is given by

$$v_d^{\mathrm{crit}}=\frac{\omega_r}{k_z}\left\{1+\frac{T_e}{T_i}\frac{v_e}{v_i}\Gamma_1(b)\exp\left[-\left(\frac{\omega_r-\Omega}{k_z v_i}\right)^2\right]\right\}, \qquad (1)$$

where v_d^{crit} is the threshold electron-drift velocity for excitation, $\omega_r=\Omega\{1+\Gamma_1(b)T_e/[T_i-G(b)T_e+T_e]\}$, k_z is the axial wavenumber, $v_\alpha^2\equiv k_B T_\alpha/m_\alpha$ is the square of the thermal speed, $b\equiv k_\perp^2\rho_i^2$, α denotes the species, Ω is the ion-cyclotron frequency, Γ_1 is the gamma function, and $G(b)\equiv\Gamma_1(b)+[1-\Gamma_0(b)]/b$. The approximately linear B-dependence of the critical drift comes from the leading factor ω_r ($\approx\Omega$). This dependence can be seen in Fig. 2 for

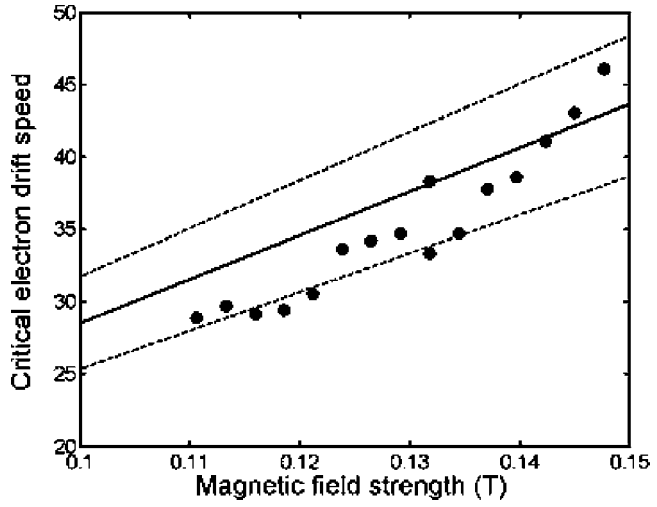

FIG. 2. Normalized critical electron drift speed $v_d^{\mathrm{crit}}/v_{\mathrm{th},i}$ for the onset of CDEIC waves in a potassium plasma as the magnetic field is varied. The lines represent a family of theoretical threshold curves without filamental quenching. Assumed values of $\lambda_z=40$ cm (bottom line), 45 cm (middle line), and 50 cm (top line) fall in the range of measured values.

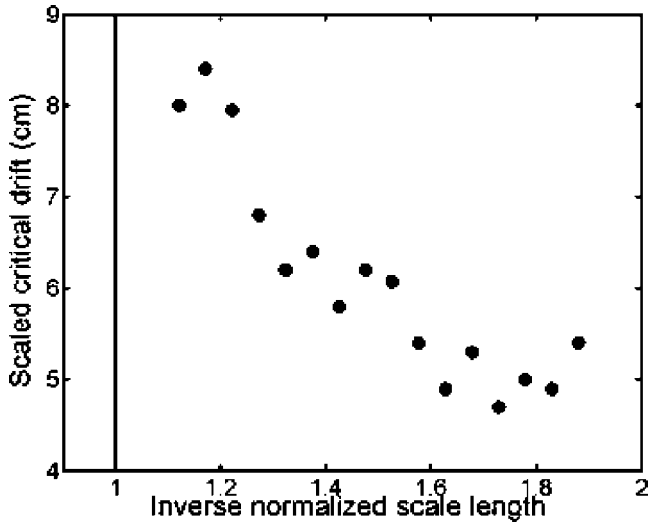

FIG. 3. Critical values of scaled electron drift K_{crit}^{-1} for the onset of CDEIC waves in a cesium plasma as the current channel size approaches the point indicated by the solid line, where $\sigma_r\{v_d\}=\rho_i$.

the case of potassium plasma in which incrementing the magnetic-field strength to larger values increases the minimum value of v_d necessary to excite CDEIC waves. In this case, the value of $\rho_i/\sigma_r\{v_d\}$ associated with the narrow current channel that maps to the button electrode (the annulus can be ignored because it is electrically floating) is small (<1) and has no detectable effect on the stability threshold. This behavior of the critical drift velocity and other important aspects of the CDEIC instability were verified by Correll *et al.*[27]

Scaling v_d^{crit} to the ion-cyclotron frequency removes this magnetic-field dependence from the expression for the excitation-threshold parameter $(K_{\mathrm{crit}})^{-1}$,

$$K_{\mathrm{crit}}^{-1} \equiv \frac{v_d^{\mathrm{crit}}}{\Omega} = \frac{1}{k_z}(1+\cdots). \tag{2}$$

Since the value of K_{crit}^{-1} is expected to be relatively insensitive to B for cases involving no change in axial wavenumber, it becomes a useful parameter for recognizing changes in the excitation threshold due to other factors. The axial wavelength λ_z is measured and found to be independent of magnetic field with value $\lambda_z=45\pm5$ cm. The phenomenon of filamental quenching is expected to increase the value of K_{crit}^{-1} when the scale size of the current channel approaches the ion gyroradius. This occurs at low magnetic-field strength in cesium plasma experiments described in this paper. Figure 3 shows K_{crit}^{-1} as a function of the current-channel diameter $\sigma_r\{v_d\}$ normalized to the cesium gyroradius for the case of equal bias applied to both segments and magnetic-field strength ranging from 0.03–0.05 T. Near $\rho_i/\sigma_r\{v_d\}\approx1$, the critical drift velocity increases to the point at which the instability threshold exceeds the drift velocity producible with the present power supply. This phenomenon is explained not by local theory but by a nonlocal theory.[1] Cartier *et al.*[2] demonstrated the existence of filamental quenching in laboratory plasma with a diverging axial magnetic field and an axially movable button.

B. Plasma equilibria

Now, we characterize the plasma equilibrium of DIDE, for conditions in which no waves were observed, and demonstrate the variations of the two normalized scale lengths $\rho_i/\sigma_r\{E_r\}$ and $\rho_i/\ell_r\{n_i\}$. Figure 4 shows an example of the radial profile of ion density n_i in Na plasma using the DIDE configuration. The annular electrode is electrically floating and the button voltage Φ_b is 22 V, where the north (south) hot-plate voltage Φ_{NHP} (Φ_{SHP})=−4 V (0 V). Here, the axial magnetic field $B=0.14$ T and n_i is measured from the ion saturation current to a translatable Langmuir probe with a collection area of 1 mm^2. The ion saturation current is measured with fixed probe bias (−20 V) relative to the local

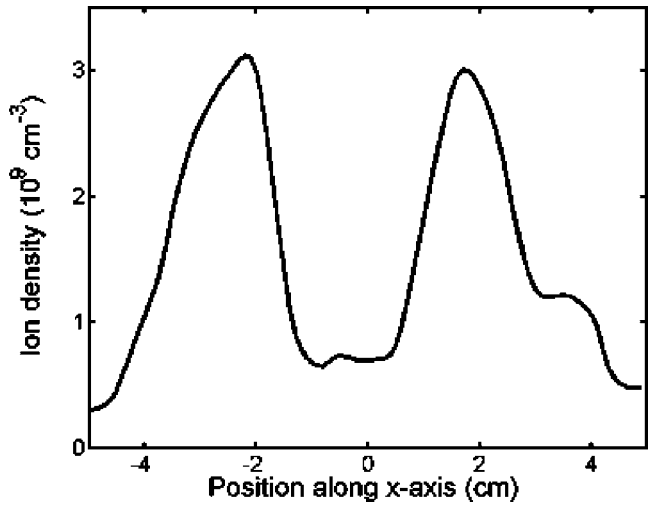

FIG. 4. Radial profile of ion density n_i, calculated from the ion saturation current of a Langmuir probe, in Na plasma.

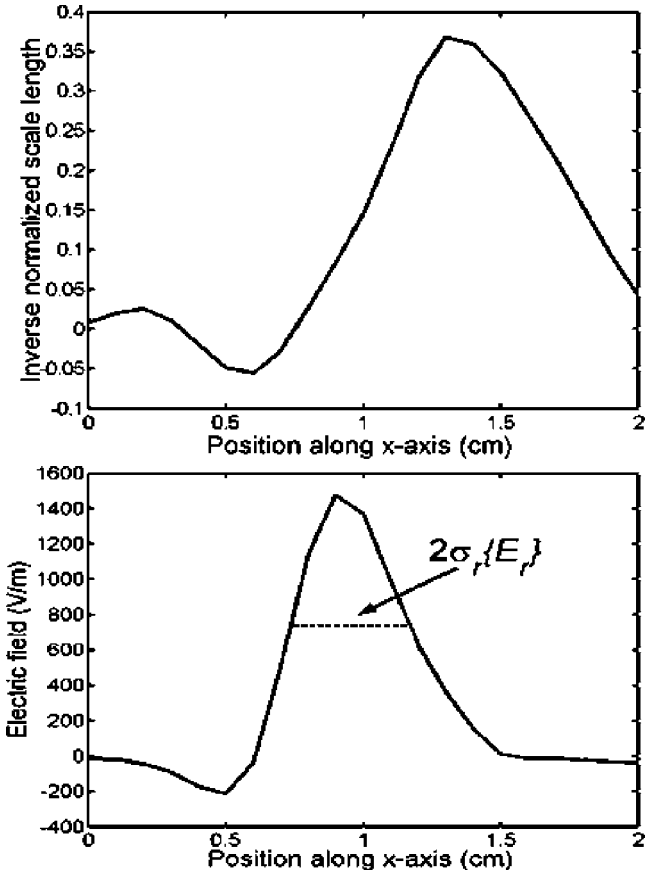

FIG. 5. Radial profile of (top) inverse normalized density-gradient scale length ρ_i/L_n in Na plasma from the profile of Fig. 2 and (bottom) electric-field amplitude showing the inhomogeneity scale length $\sigma_r\{E_r\}$.

floating potential of the Langmuir probe. Figure 5(a) shows ρ_i/L_n as a function of the position in the inner coaxial region (positive-x side is shown) using the profile of Fig. 4 in the calculation. The maximum value of $\rho_i/L_n(r)=0.37$ in this case. The electric field, as derived from the plasma potential $\phi(x)$ inferred from the floating potential of a translatable emissive probe,[28] is shown in Fig. 5(b). Here, Φ_{NHP} is changed slightly from the value used in Fig. 5(a), from -4 to -3 V, and the full-width at half-maximum $\sigma_r\{E_r\}$ is shown for reference. In this case, $\rho_i/\sigma_r\{E_r\}$ becomes 0.16 cm/0.22 cm=0.73.

In this experiment, the gradients in plasma potential and density were always oppositely directed. An attempt was made to produce two equilibria, each with the density and potential gradients in the same direction (i.e., both outward or both inward directed) by supplying an excess flux of alkali metal vapor to one source (thus increasing the ion production of that source) for a given differential bias applied between the hot plates. This led to a change in the radial profiles of both potential and density such that the gradients in potential and density always remained oppositely directed. We speculate that the equilibrium cases associated with the missing two combinations of the signs of $\mathrm{d}\phi/\mathrm{d}r$ and $\mathrm{d}n/\mathrm{d}r$ might be attainable by the transient control of the potential. Note that the relation between potential and ion density is more complicated than given by the Boltzmann relation; however, it does follow the basic trend of increased (decreased) ϕ leading to decreased (increased) n_i. It will be shown in Sec. IV that the radial profile of ion density is a consequence of the particle orbits in the strongly inhomogeneous radial electric field.

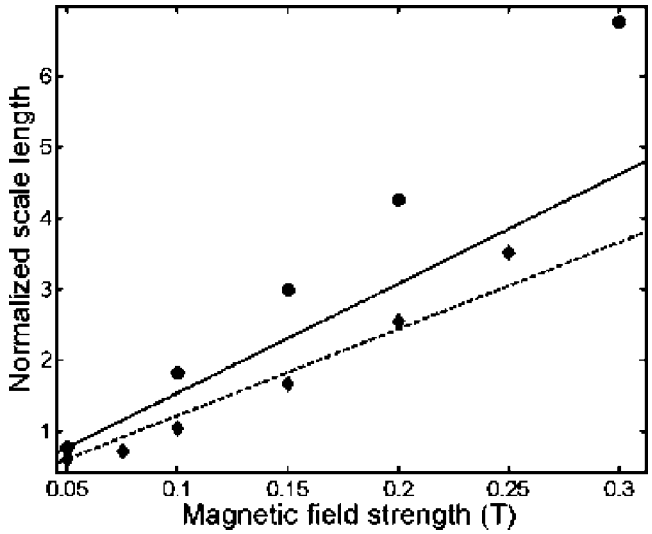

FIG. 6. Magnetic-field dependence of $\sigma_r\{E_r\}/\rho_i$ (closed diamonds) and $\ell_r\{n_i\}/\rho_i$ (closed circles) in Na plasma. Dotted (solid) line represents expected magnetic-field dependence if $\sigma_r\{E_r\}$ ($\ell_r\{n_i\}$) were held constant.

By varying the magnetic field, wide ranges of $\rho_i/\sigma_r\{E_r\}$ and $\rho_i/\ell_r\{n_i\}$ were obtained in sodium plasma. These data are shown in Fig. 6, where the inverse ratios $\sigma_r\{E_r\}/\rho_i$ and $\ell_r\{n_i\}/\rho_i$ are plotted. Plotting the inverse allows the reader to readily observe changes in the inhomogeneity scale lengths as a departure from the straight line associated with changes in ρ_i. Here, the annular electrode is electrically floating and $\Phi_b=22$ V with Φ_{NHP} (Φ_{SHP})$=-1.2$ V (-2.0 V), and $\rho_i/\ell_r\{n_i\}$ is re-measured at each value of magnetic field. By increasing the magnetic field from 0.05 to 0.25 T, $\sigma_r\{E_r\}/\rho_i$ is raised from 0.56 to 3.3. The dashed line represents the expected trend in the case of constant $\sigma_r\{E_r\}$. The data do not vary much from the dashed line, which implies that $\sigma_r\{E_r\}$ varies very little as the magnetic-field strength is increased. There is, however, some variation from the straight line that we cannot explain. The case of constant $\sigma_r\{E_r\}$ is realistic since the electrons are primarily responsible for the plasma potential profile. Since the electrons have small gyroradii and negligible collisionality, the *shape* of the plasma potential profile, and consequently the *shape* of the electric-field profile, is only weakly dependent on magnetic-field strength. It will be shown later that the *magnitude* of the electric-field profile is sensitive to the magnetic-field strength for electric fields produced by the segmented-disk electrode. On the other hand, the shape of the *density* profile depends on the magnetic-field strength. By increasing the magnetic field from 0.05 to 0.3 T, $\ell_r\{n_i\}/\rho_i$ is raised from 0.77 to 6.67. The solid line represents the expected trend if $\ell_r\{n_i\}$ is constant. Since the measured values of $\ell_r\{n_i\}/\rho_i$ increase more quickly than the predicted values (solid line) as magnetic-field strength increases, $\ell_r\{n_i\}$ must increase with increasing magnetic-field strength. Even though the density gradients increase for increasing magnetic-field strength (due to the

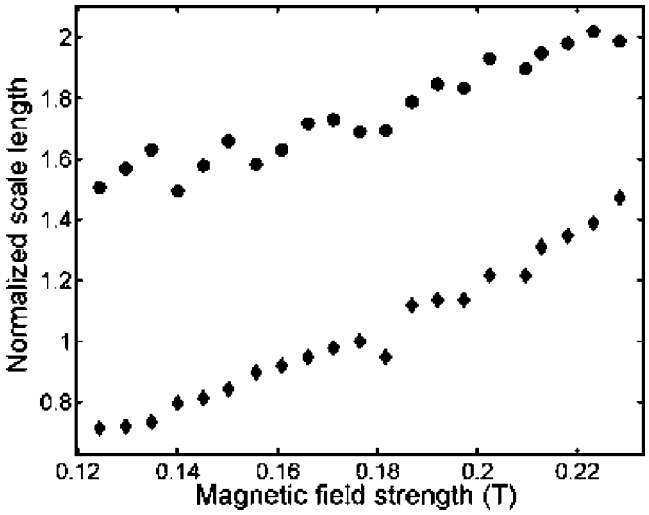

FIG. 7. Magnetic-field dependence of $\sigma_r\{E_r\}/\rho_i$ (diamonds) and $\sigma_r\{V_\theta\}/\rho_i$ (circles) for electric-field generation by a positively biased electrode in potassium plasma. $\sigma_r\{V_\theta\}/\rho_i$ is calculated from the ion-drift profile results obtained from the test-particle simulation.

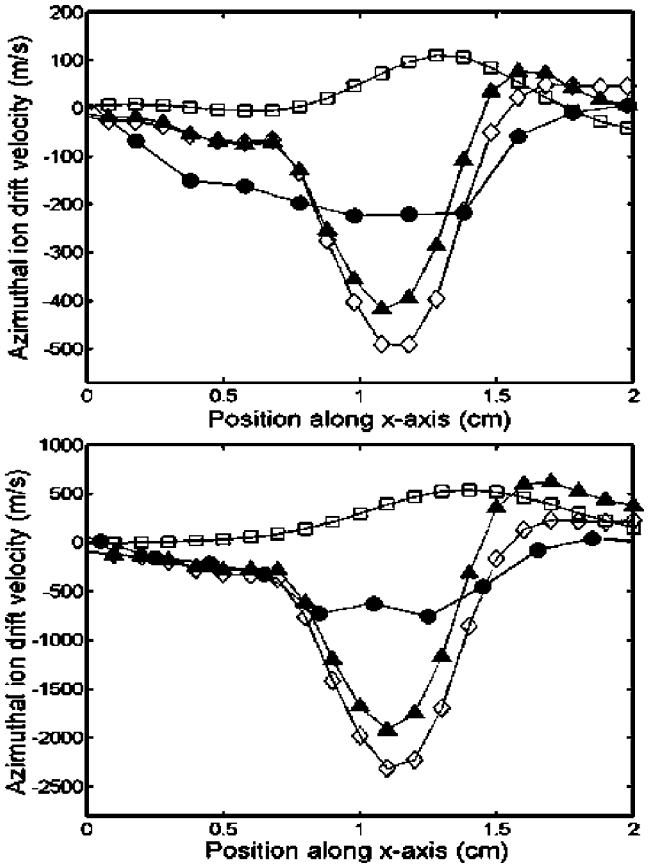

FIG. 8. Radial profiles of various azimuthal ion drifts in Ba plasma for (top) low-electric-field case ($E_{max}=150$ V/m) and (bottom) high-electric-field case ($E_{max}=670$ V/m). Here is shown LIF-measured drift (closed circles), $\mathbf{E}\times\mathbf{B}$ drift (open diamonds), pressure-gradient drift (open squares), and the sum of $\mathbf{E}\times\mathbf{B}$ plus pressure-gradient-drift velocity (closed triangles).

decrease in ion gyroradius), the ion density increases even more rapidly and results in an increase in $\ell_r\{n_i\}$.

Next, the effect of Φ_b on $\rho_i/\sigma_r\{E_r\}$ and $\rho_i/\ell_r\{n_i\}$ is investigated in Ba plasma. Here, $B=0.28$ T, the annular electrode is electrically floating, and Φ_{NHP} (Φ_{SHP})$=-1.2$ V (-2 V). The effect of Φ_b, ranging from 6 to 10 V, on $\rho_i/\sigma_r\{E_r\}$ ($\rho_i/\ell_r\{n_i\}$) is weak (moderate), i.e., from 0.96 (1.28) to 0.92 (1.12), which is a 4% (13%) drop. This suggests that individual control of $\rho_i/\sigma_r\{E_r\}$ and $\rho_i/\ell_r\{n_i\}$ may be possible over a small range, although they cannot be controlled over a wide range as discussed before.

The localization of the radial electric field generated by differentially biasing the segmented electrode was investigated for potassium plasma. The results are shown in Fig. 7, where $\sigma_r\{E_r\}/\rho_i$ increases approximately linearly with magnetic-field strength. For comparison, the half-width at half-maximum of the ion-drift profile $\sigma_r\{V_\theta\}$, as calculated with the test-particle simulation, is plotted as $\sigma_r\{V_\theta\}/\rho_i$. Again we chose to plot $\sigma_r\{E_r\}/\rho_i$ and $\sigma_r\{V_\theta\}/\rho_i$ for ease of comparison, while we will stick to discussing their inverse throughout the rest of the paper. Even though the difference between the two data sets decreases with increasing magnetic-field strength, the ion-flow profile is significantly broader than the electric-field profile at all values of magnetic-field strength used in this experiment. It is expected that the two scale lengths would become equal for sufficiently large magnetic-field strength. In an experiment where the details of the ion-flow profile are important in calculations of plasma stability, inhomogeneity scale lengths should be evaluated to ensure that finite-Larmor-radius effects are well understood and properly incorporated into the interpretation.

C. Rotation profile

Here, results of the equilibrium ion-flow profile in the DIDE configuration are presented. Langmuir probe and emissive probe measurements have a spatial resolution of 1 mm while LIF measurements have a spatial resolution of $\Delta x=1$ mm and $\Delta y=1.5$ mm. For the flow profiles presented in this section, i.e., $B=0.187$ T, both disk and annular electrode segments are electrically floating, and Φ_{NHP} (Φ_{SHP})$=-0.1$ (0) V and -2 (0) V for Figs. 8(a) and 8(b), respectively. In this configuration, no waves are observed and, thus, wave particle interactions can be neglected in the analysis of the equilibrium. In Fig. 8(a) the radial profile of azimuthal velocity is shown as measured with LIF (V_{LIF}), as calculated from the radial electric-field profile ($V_{\mathbf{E}\times\mathbf{B}}$), as calculated from the radial profile of density (V_{∇_p}), and as calculated from the sum $V_{sum}=V_{\nabla_p}+V_{\mathbf{E}\times\mathbf{B}}$. For this case, $\rho_i/\sigma_r\{E_r\}=1.3$, $\rho_i/\ell_r\{n_i\}=0.45$ and the maximum electric field E_r is 150 V/m as calculated from the radial profile of plasma potential measured with an emissive probe. The signs of V_{LIF} and $V_{\mathbf{E}\times\mathbf{B}}$ are opposite to that of V_{∇_p}; thus, the diamagnetic drift reduces the total calculated ion drift to less than the $\mathbf{E}\times\mathbf{B}$ drift. In this case, there is a substantial difference between V_{LIF} and V_{sum}. The difference between V_{sum} and V_{LIF} comes from the fact that the Ba ions sample a large portion of the radial electric-field profile during gyrations because $\sigma_r\{E_r\}$ (0.22 cm) is smaller than ρ_i (0.29 cm). Figure 8(b) shows the various azimuthal rotation velocities in the case of strong field E_r of 670 V/m. In this case,

$\rho_i/\sigma_r\{E_r\}=1.3$ and $\rho_i/\ell_r\{n_i\}=0.63$. Ion drift velocity, calculated by test-particle simulation, V_{sim}, agrees well with V_{LIF}, as will be shown in Sec. IV.

IV. TEST-PARTICLE SIMULATION

A. Concept

Fluid approximations are commonly employed in the calculation of the perpendicular ion-drift-velocity profile when there are gradients in plasma potential and density. For many cases where finite-Larmor-radius effects must be taken into account, it suffices to apply the operator[29] $(1+\rho_i^2\nabla^2)$ to the zero-order drift-velocity expressions. However, as $\rho_i/\sigma_r\{E_r\}$ and $\rho_i/\ell_r\{n_i\}$ become close to or larger than unity, this treatment breaks down as the above operator is a truncated expansion in even powers of $\rho_i/\sigma_r\{E_r\}$, where odd powers of $\rho_i/\sigma_r\{E_r\}$ are averaged to zero by the gyromotion. The test-particle simulation described here addresses this problem in slab geometry by calculating the ion distribution function $f(x,v_y)$ for an arbitrary electric-field profile $E_x(x)$. From $f(x,v_y)$, we can calculate the moments to obtain the density, drift velocity, and temperature.

Calculating the phase-space density of an entire species $f(x,v_y)$ begins with the determination of the phase-space trajectory of a single particle and repeating this for an ensemble of identical particles with the proper distribution of initial conditions. Conveniently, the phase-space trajectory of a particle with arbitrary initial conditions x_i, y_i, $v_{x,i}$, and $v_{y,\text{i}}$ forms a closed orbit in the x-v_y plane making the determination of the phase-space density straightforward. Finally, the full phase-space density $f(x,v_y)$ is built up by summing all the single-particle phase-space densities in the x-v_y phase space.

In practice, the x-v_y phase-space density is represented by amplitude on a uniformly divided two-dimensional grid (with each grid point representing a small area $\Delta x\Delta v_y$ in the x-v_y plane). First, each particle is tracked through a complete orbit using N steps in x and v_y. Next, the N particle positions in the phase space are binned, with normalization $1/N$, into the closest points on the phase-space grid. The normalization ensures that the total probability of finding the particle anywhere in the phase space is unity. A large number of particles ($\geqslant 10^5$) are loaded into the phase space with initial conditions that depend on how the particles are introduced into the electric-field region. It will be shown that a given electric-field profile has more than one ion-flow equilibrium possible depending on how the ions are introduced into the electric field.

B. Effect of adiabatic versus nonadiabatic evolution of equilibrium on ion dynamics

An adiabatic increase in electric-field strength results in an increase in ion-drift speed without an increase in the ion oscillatory velocity. This effect has been demonstrated in previous work,[30] but the importance of the ion's initial position within the electric-field structure was not addressed. In the following analysis, initial position of an ion within a Gaussian electric-field profile, along with the subsequent polarization shift, will be included. Evolution of ion dynamics in an adiabatically increasing electric field is demonstrated in Fig. 9, where v_y is plotted versus time for four initial conditions $v_y=0$, $v_x=0$, $x=(0,-1/3\sigma_x\{E_x\},-2/3\sigma_x\{E_x\},-\sigma_x\{E_x\})$, and a time-dependent electric-field $E=E_o\tanh(t/T)$, where T is much larger that the ion-cyclotron period. The parameters used in this numerical solution were adjusted such that the net polarization shift for a uniform electric field (given by $E_o/(B\Omega)$) is equal to $\sigma_x\{E_x\}$. The class of ions that start at $x=0$ shift into a region of smaller electric-field strength, while the class of ions that start at $x=-\sigma_x\{E_x\}$ shift into a region of larger electric-field strength, resulting in a larger net drift speed for the ion population.

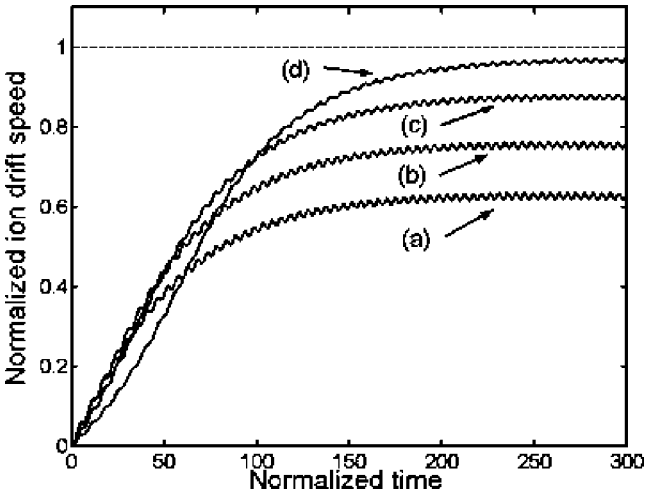

FIG. 9. Ion speed V_y as a function of normalized time (Ωt) for an adiabatic increase in electric-field strength with polarization shift $E_0/(B\Omega)=\sigma_x\{E_x\}$. Four lines are plotted for ions starting at (a) x=0, (b) $x=-\sigma_x\{E_x\}/3$, (c) $x=-2\sigma_x\{E_x\}/3$, and (d) $x=-\sigma_x\{E_x\}$. Here, $\Omega T=100$ and $(v_y-\langle v_y\rangle)/(E/B)=0.008$.

If the ions experience an instantaneous (i.e., nonadiabatic) onset of the electric field, then there will be a substantial gain in the oscillatory velocity of the ions and they will

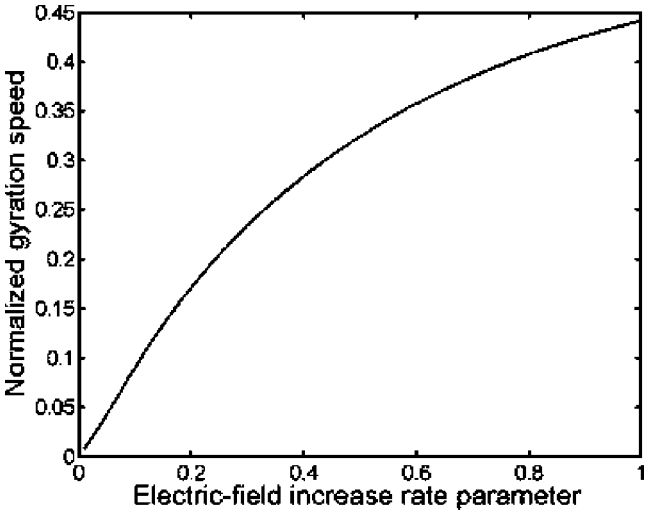

FIG. 10. Increase in ion gyration speed (normalized to E_0/B) as a function of $1/(T\Omega)$, where T governs the rate of increase in electric-field strength as $E=E_0\tanh(t/T)$. The electric-field profile is the same as in Fig. 9 with initial conditions $x=0$ and $v_y=v_x=0$.

have an effectively larger gyroradius. The dependence of the gain in oscillatory velocity was shown by Gavrishchaka[31] to increase linearly with T for uniform electric field. The dependence of this particle energization on the rate of increase in electric-field strength, for a Gaussian electric-field profile, is illustrated in Fig. 10 (for the same parameters as in Fig. 9), where $[(v_y - \langle v_y \rangle)/(E_o/B)]_{\max}$ is plotted versus $1/(\Omega T)$, as calculated from a numerical solution to the equations of motion for a particle starting with zero velocity at $x=0$. Thus, the equilibrium ion-flow profile generated by a nonadiabatic increase in electric-field strength is characterized by an elevated perpendicular ion temperature.

For the cases described in the previous paragraph, the initial value of the electric field is zero and the particles are loaded into the test-particle simulation with initially uniform density, uniform temperature, and no drift. However, if the ions experience an adiabatic increase in $\rho_i/\sigma_x\{E_x\}$ (i.e., either the magnetic-field strength or $\sigma_x\{E_x\}$ is decreased on a time scale that is long compared to the ion-cyclotron period) while the electric-field magnitude is held constant, then the ions are loaded into phase space distributed according to the following equation:[3]

$$f_{0\perp} = \beta \exp\left[-\frac{\beta}{2}\left(v_x^2 + \frac{[v_y - V_E(x)]^2}{\eta(x)} \right) \right] [\eta(x)]^{-1/2}, \qquad (3)$$

where $\beta = 1/v_{\mathrm{th},i}^2$, $V_E = -E(x)/B$, $\eta(x) = [1 + V_E'(x)/\Omega]$, $v_{\mathrm{th},i}^2 = k_B T_i/m_i$, m_i is the ion mass, k_B is Boltzmann's constant, Ω is the ion-cyclotron frequency, and the prime denotes differentiation with respect to x. Equation (3) is the first-order (in $\rho_i/\sigma_x\{E_x\}$) solution for plasma with an inhomogeneous, perpendicular electric field. Thus, the above loading assumes $\rho_i/\sigma_x\{E_x\} \ll 1$ as the initial condition so that Eq. (3) is initially a correct equilibrium distribution. If the plasma under investigation had a gradient in temperature or density, before application of the electric field, Eq. (3) could be straightforwardly modified, based on the constants of motion, to include the effect of these gradients. The ions are tracked through many cyclotron periods until $\rho_i/\sigma_x\{E_x\}$ is increased adiabatically to the final value, after which the phase-space densities of the resulting orbits are calculated.

C. Velocity profile

The two experimental configurations described in this paper have significantly different characteristics owing to the fact that the introduction of the ions into the electric-field structure is effectively adiabatic for one configuration and instantaneous for the other. When the localized electric field is produced by a positively biased, segmented-disk electrode, the electric-field strength effectively increases adiabatically (in the frame of the ion) from zero at the hot-plate surface to some maximum value at larger z, beyond the hot-plate sheath. This is evidenced by LIF measurements that indicate a perpendicular ion temperature of 0.2 eV both before and after application of the electric field. On the other hand, the DIDE configuration produces an electric field that is effectively instantaneous in the frame of an ion as it passes one of the electrodes and into the electric-field region. This is evident in the increase in ion temperature observed in the LIF measurement where ion temperatures as large as 1 eV have been observed. The perpendicular ion-temperature increase in the DIDE configuration is generally linear with increasing electric-field strength, as expected, but is larger in magnitude, by almost a factor of 2, than is predicted by the test-particle simulation. Since no waves were observed in this experiment, the increase in ion temperature cannot be explained by wave-induced ion heating. This anomalously large (i.e., unexplained) increase of the ion oscillatory velocity is the subject of continuing research and is being exploited to study the effects of ion-temperature anisotropy.

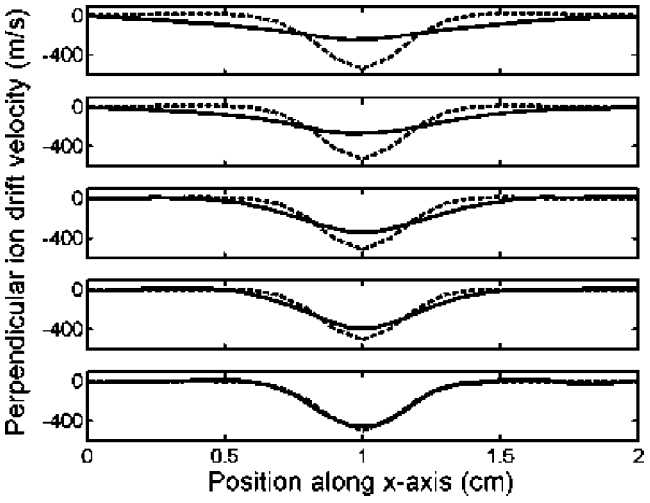

FIG. 11. Radial profile of V_y from the test-particle simulation as calculated from the first moment of the velocity distribution function (solid line) compared to V_y as calculated from fluid theory (dashed line) for $a=0.2$ cm, $E_0=100$ V/m, $B=0.2$ T, $T_i=0.2$ eV, and $x_0=1.0$ cm. The ion species are, from top to bottom, Ba, Rb, K, Na, and Li, for which $\rho_i/\sigma_x\{E_x\}$ values are 1.58, 1.24, 0.84, 0.65 and 0.36, respectively.

The ion-velocity profiles shown in Figs. 8(a) and 8(b) are azimuthal ion flows in a cylindrically symmetric system. Cylindrical effects have been calculated and are found to be negligible $[V_\theta/(r\Omega) \ll 1]$. Thus, it is sufficient to use slab geometry to model the ion flows in the experiment presented here. For the test-particle simulation the electric-field profile is modeled by fitting a Gaussian electric-field profile $E(x) = E_0 \exp[-(x-x_0)^2/a^2]$ to the electric field determined from the measured potential profile $\phi(x)$. It is found that a Gaussian fits the measured electric-field profile well. An important point in modeling the electric field this way is to make sure the potential drop $\Delta\phi$, as measured across the electric-field layer with the emissive probe, is properly represented. To ensure this, the additional constraint $E_0 a\sqrt{\pi} = \Delta\phi$ is placed on the fit.

To demonstrate the effect of $\rho_i/\sigma_x\{E_x\}$ on the ion-flow profile, the test-particle simulation has been run for an adiabatically increasing electric-field profile with $a=0.2$ cm, $E_0=100$ V/m, $B=0.2$ T, and $x_0=1.0$ cm. The simulation was run for five different ion masses corresponding to Ba, Rb, K, Na and Li, all of which are applicable to Q-machine plasma. These parameters cover a range in $\rho_i/\sigma_x\{E_x\}$ from 0.36 to 1.58. The corresponding ion-velocity profiles are shown in Fig. 11, along with the sum of $\mathbf{E}\times\mathbf{B}$ plus diamagnetic drift velocities calculated from fluid theory. For Li, $\rho_i/\sigma_x\{E_x\}$

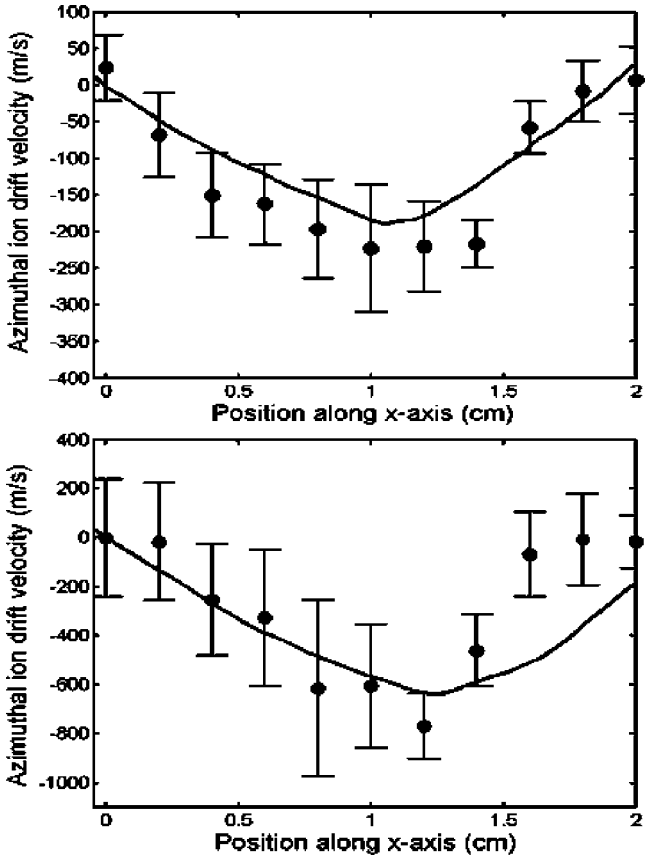

FIG. 12. Comparison between LIF-measured drift profile (circles) and simulation calculated drift profile (solid line) for (top) profile from Fig. 8(a) and (bottom) profile from Fig. 8(b).

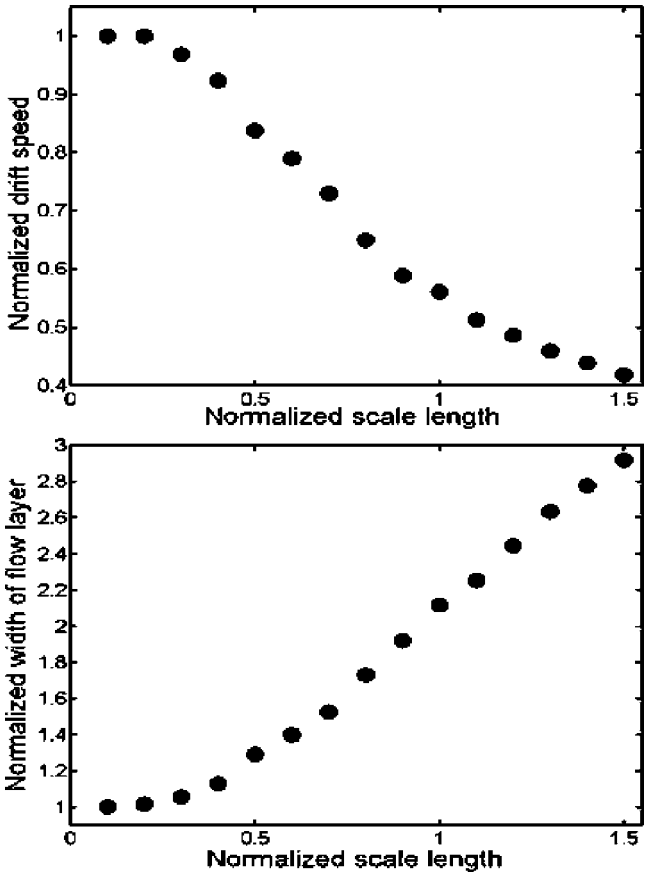

FIG. 13. Dependence on $\rho_i/\sigma_x\{E_x\}$ of (top) the ratio of the maximum ion-drift speed from simulation to the maximum ion-drift speed calculated from fluid theory and (bottom) the ratio $\sigma_x\{V_y\}/\sigma_x\{E_x\}$.

$=0.36$ and the ion velocity is modeled fairly well by fluid theory. However, for heavier ion mass, $\rho_i/\sigma_x\{E_x\}$ becomes larger and the ion drift is not modeled well by fluid calculations. In fact, for larger $\rho_i/\sigma_x\{E_x\}$, nonzero ion drift exists for all $|x|<x_0$, where even fluid theory with FLR corrections would predict zero drift. This drift can be understood by considering the distance a particle, with arbitrary $(v_{x,i}v_{y,i})$ and loaded a distance Δx to the left of the electric-field layer, will travel along the positive x axis in the absence of an electric field. The question is whether the particle will reach the electric-field layer (i.e., will the particle travel a distance greater than Δx along the x axis)? The particle will travel a distance $\rho_i(1+v_y/|\vec{v}|)$ toward the electric-field layer and thus will make it to the electric-field layer only if the y component of its velocity satisfies the following inequality:

$$\frac{v_y}{\Omega} \geqslant (\Delta x - \rho_i), \tag{4}$$

where $\vec{v}$ is the initial velocity vector. For typical electric-field magnitudes in our experiment, particles that enter the electric-field layer make a large excursion beyond the layer due to acceleration by the electric field. This leads to depletion of the ion phase-space density for $x<x_0$. This will be discussed in detail in the next section where the density profile is shown to be a consequence of particle orbits in the inhomogeneous electric-field structure. It is obvious from Eq. (4) that, for a given Δx, this depletion selects particles with sufficiently positive v_y, leaving the local velocity distribution function with a net negative drift. For larger values of Δx (i.e., farther from the electric-field layer), fewer particles satisfy Eq. (4), resulting in less depletion and smaller net drift.

The simulation was performed with a nonadiabatic electric-field increase for the two cases shown in Figs. 8(a) and 8(b). For the first case, corresponding to Fig. 8(a), the simulation was run with $a=0.17$ cm, $E_0=152$ V/m, $m_i=137$ amu, $B=0.187$ T, and $x_0=1.0$ cm. For the second case, corresponding to Fig. 8(b), the simulation was performed with $a=0.20$ cm, $E_0=671$ V/m, $m_i=137$ amu, $B=0.187$ T, and $x_0=1.0$ cm. As mentioned before, these quantities are calculated based on the measured electric-field profile. The ion-drift profiles, from the simulation, are compared to the LIF-measured ion-drift profiles for the first and second cases in Figs. 12(a) and 12(b), respectively. The simulation reproduces the main features of the measured ion-drift profile for $r<1.5$ cm, including the nonzero drift in the inner region (i.e., for $x<x_0$). Outside $r=1.5$ cm, there exist small electric fields not accounted for in the simulation. The value of $\rho_i/\sigma_r\{E_r\}=1.3$ for the above cases is far below the largest values observed in the experiment. This case was chosen because it shows the FLR effects clearly while retaining

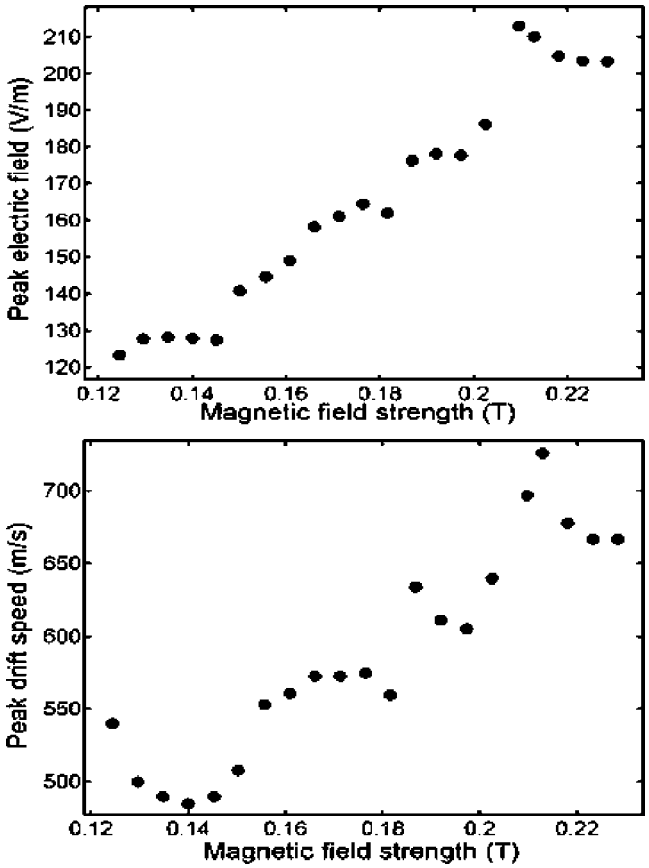

FIG. 14. Magnetic-field dependence of (top) the measured electric-field peak magnitude and (bottom) ion-drift-speed maximum as calculated from the test-particle simulation. Electric fields generated by a positively biased electrode increase linearly with magnetic field. The combined effects of increasing electric-field magnitude and decreasing $\rho_i/\sigma_r\{E_r\}$ (as B is increased) leads to an increase in the ion perpendicular drift magnitude.

structure in the ion flow. For the largest case, i.e., $\rho_i/\sigma_r\{E_r\}=4.6$, the ion-drift profile shows very little structure.

To quantify the effect of $\rho_i/\sigma_x\{E_x\}$ on the ion-drift profile, the test-particle simulation was run, as a function of ion temperature, for an adiabatically increasing electric field. By varying the temperature, the gyroradius and, consequently, $\rho_i/\sigma_x\{E_x\}$ change, while all other parameters remain constant. The simulation for these cases is performed for a single Gaussian electric-field profile with $B=0.7$ T, $E_{\max}=1000$ V/m, $m_i=137$ amu, and $a=0.5$ cm. In Fig. 13(a), the calculated peak ion drift is normalized to the calculated peak $\mathbf{E}\times\mathbf{B}$ drift and plotted versus $\rho_i/\sigma_x\{E_x\}$. For $\rho_i/\sigma_x\{E_x\}=1$, the normalized ion drift is reduced to almost 50% of the peak value. The results of Fig. 13(a) are consistent with the results of Gavrishchaka,[24] where $(v_y-\langle v_y\rangle)/V_{\mathbf{E}\times\mathbf{B}}$ is plotted versus increasing $V_{\mathbf{E}\times\mathbf{B}}/(\sigma_x\{E_x\}\Omega)$ for a single particle in a "top-hat" electric-field profile. In Fig. 13(b), the ratio $\sigma_x\{V_y\}/\sigma_x\{E_x\}$ is plotted versus $\rho_i/\sigma_x\{E_x\}$. For $\rho_i/\sigma_x\{E_x\}=1$, the ion-drift profile width is increased to more than double the electric-field profile width. Combining these two effects gives a reduction of the maximum shear, for $\rho_i/\sigma_x\{E_x\}=1$, in the ion-drift profile to ~25% of that which would be calculated based on fluid theory. Thus, calculations of the ion-drift

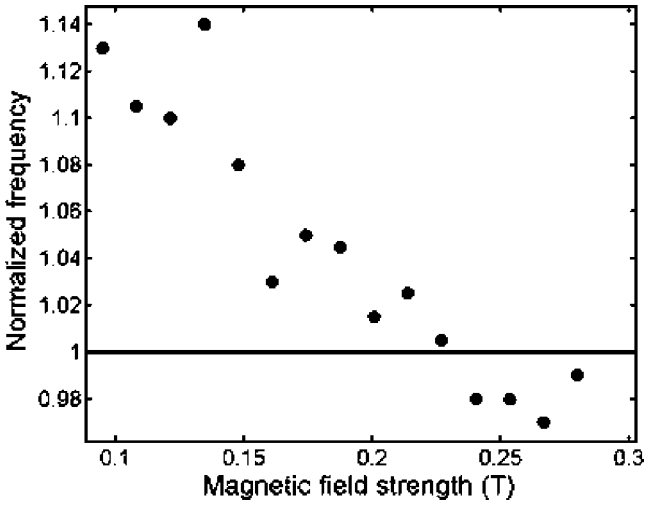

FIG. 15. Mode frequency normalized to the ion cyclotron frequency as a function of magnetic-field strength in potassium plasma. The solid line indicates the ion-cyclotron frequency.

profile based on the fluid equations and the measured density and electric-field profiles will give an increasingly wrong answer for increasing $\rho_i/\sigma_x\{E_x\}$.

For the case of Fig. 7 (electric-field generation by a positively biased, segmented-disk electrode), measurement of the electric-field profile indicates that the electric-field magnitude increases approximately linearly with magnitude-field strength as shown in Fig. 14(a). This is not observed in the DIDE configuration. The measured electric-field strength and localization from Fig. 7 were used in the test-particle simulation to calculate the maximum value of ion drift expected for the equilibrium conditions and an adiabatic increase in electric-field strength. This peak ion drift is shown in Fig. 14(b) as a function of magnetic field. The peak ion drift increases with magnetic-field strength due to the increasing electric-field magnitude and the decreasing value of $\rho_i/\sigma_x\{E_x\}$. This means the equilibrium is becoming more fa-

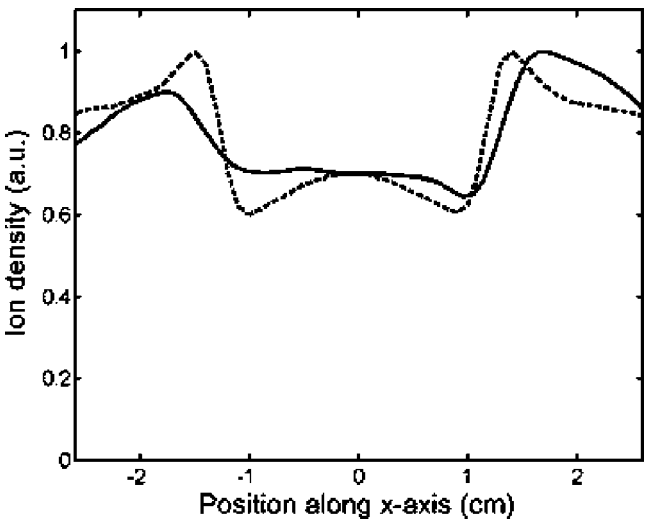

FIG. 16. Comparison between ion density obtained from the ion saturation current to a Langmuir probe (solid line) and the ion density calculated from simulation for the case of Fig. 6(a).

vorable to IEDDI since the IEDDI mechanism depends directly on both the magnitude of perpendicular ion drift and the localization. Figure 15 shows the normalized mode frequency versus magnetic-field strength for potassium plasma for a larger range of magnetic-field strength. The decrease in normalized mode frequency to less than unity is indicative of a transition from CDEIC to IEDDI. The transition from IEDDI to CDEIC that occurs as the magnetic field is reduced is due to the simultaneous shrinking of the peak ion drift and increase in $\rho_i/\sigma_x\{E_x\}$, both of which create less favorable conditions for the IEDDI mechanism. Thus, the shrinking of the electric field relative to the ion gyroradius reduces the IEDDI mechanism to the point that the mode character becomes that of CDEIC. For larger values of E/B, IEDDI might be quenched in favor of the EIH instability but the later instability has only been observed in the WVUQ for much larger values of E/B than exist in the present experiment.

D. Density profile

In the test-particle simulation, an initially homogeneous distribution of particle positions, loaded into an inhomogeneous electric field, results in equilibrium with an inhomogeneous density profile. This is illustrated in Fig. 16, where the density calculated from the simulation run for Fig. 12(a) (dashed line) is compared to the density derived from the ion saturation current (solid line) of a scanning Langmuir probe. The depletion observed in the simulation density profile for $-1\ \text{cm} < x < 1\ \text{cm}$ agrees, in magnitude, with the depletion observed in the measured ion-density profile. This result of the simulation supports the interpretation that the density depletion is due mainly to the finite-Larmor-radius particle trajectories in the presence of an inhomogeneous electric-field profile, as opposed to diffusion of ions from regions of higher potential to regions of lower potential.

The simulation overestimates the magnitude of density gradients, as can be seen by comparing the density profiles of Fig. 16. This is likely due to the collisionless approximation made in the simulation. In the experiment, the ion-ion collision frequency ν_{ii}, for plasma densities in the range $(1-10)\times 10^9\ \text{cm}^{-3}$, is a non-negligible fraction of the ion-cyclotron frequency (i.e., for $n_i = 3\times 10^9\ \text{cm}^{-3}$, $T_i = 0.2$ eV, and $B = 0.2$ T, $\nu_{\text{ii}}/\Omega \cong 0.1$) and thus some reduction of sharp ion-density gradients, generated by the electric-field structure, should be expected in the experiment.

V. CONCLUSIONS

In a magnetized, double-ended Q-machine, wide ranges of radial inhomogeneity scale length of both the radial electric field and the ion density have been successfully measured and interpreted quantitatively. In Na plasma, $\rho_i/\sigma_r\{E_r\}$ ($\rho_i/\ell_r\{n_i\}$) was changed from 0.4 (0.15) to 2.9 (1.3) and in Ba plasma, $\rho_i/\sigma_r\{E_r\}$ ($\rho_i/\ell_r\{n_i\}$) was controlled in a range from 0.8 (0.45) to 4.6 (2.2) by varying the magnetic field. In Ba plasma, it is shown that the scale length of the density (electric field) is weakly (moderately) dependent on the bias voltage of the central electrode. In this case, the scale length of the ion-density gradient is more sensitive to the electrode bias. In the case of a scale length of the electric field being on the order of the ion Larmor radius, we demonstrate that the azimuthal plasma-rotation velocity measured by LIF is lower than the sum of the $\mathbf{E}\times\mathbf{B}$ and ion-pressure-gradient drift velocities and we demonstrate that the net-drift profile are less radially localized than the electric-field profile. We find that the difference between the measured and fluid-theory-calculated values of the maximum of ion drift is attributed to finite-Larmor-radius particle trajectories in the presence of a strong, inhomogeneous electric-field structure. Test-particle simulation supports this interpretation by reproducing the main features of the measured ion-drift-velocity profile. In addition, the measured density depletion of the inner plasma population is explained by test-particle simulation to be a consequence of finite-Larmor-radius particle orbits in the presence of a strong, inhomogeneous electric-field structure.

Ions can be introduced into an inhomogeneous electric field on time scales that result in either an adiabatic or nonadiabatic increase in electric-field strength as viewed from the ion frame of reference. The rate of increase of the electric-field strength has important consequences for the resulting ion equilibrium. For an adiabatic increase, the ions gain no additional oscillatory energy and thus remain more localized (i.e., the gyroradius does not increase). For a nonadiabatic increase in electric-field strength the ion oscillatory energy can increase significantly, resulting in a larger gyroradius and thus a larger value of $\rho_i/\sigma_r\{E_r\}$. This leads to a decrease in maximum ion-drift speed and a broadening of the ion-flow profile as compared to the adiabatic case. In the present Q-machine experiments, both adiabatic and nonadiabatic increases in electric-field strength were obtained, as evidenced by LIF measurements of the perpendicular ion temperature and the resultant ion-flow profiles.

The magnetic-field strength affects both the CDEIC excitation threshold in field-aligned current (since v_d is proportional to B) and the degree of filamental quenching of both the CDEIC and IEDD instabilities, since both $\rho_i/\sigma_r\{E_r\}$ and $\rho_i/\sigma_r\{v_d\}$ are inversely proportional to B. By using ions with two different masses and varying B, four interesting regimes of behavior are identified. In the first, IEDDI waves are quenched and CDEIC waves are unstable (cesium plasma, high B). In the second, IEDDI waves are still quenched but CDEIC waves are also being quenched, but only partially (cesium plasma, low B). In the third, neither CDEIC waves nor IEDD waves experience quenching, yet CDEIC waves dominate since the excitation threshold is exceeded; i.e., $v_d/v_d^{\text{crit}} > 1$ (potassium plasma, low B). In the fourth, no quenching takes place but IEDD waves dominate since $v_d/v_d^{\text{crit}} < 1$ (potassium plasma, high B). Figure 15 is an example of the transition from CDEIC waves ($\omega \approx 1.1\omega_{\text{ci}}$) at low magnetic-field strength (regime #3) to IEDD ion-cyclotron waves ($\omega < \omega_{\text{ci}}$) at higher magnetic-field strength (regime #4).

ACKNOWLEDGMENTS

We gratefully acknowledge a helpful discussion about the test-particle simulation with Dr. G. Ganguli and Dr. S.

Slinker. We acknowledge helpful advice from Sean Finnegan on the implementation of the test-particle simulation code. One of us (S.S.) acknowledges greatly appreciated encouragement from Professor Y. Kawai.

This work is supported by the U.S. National Science Foundation and the U.S.-Japan Exchange Program (No. FP5-38).

[1] P. Bakshi, G. Ganguli, and P. J. Palmadesso, Phys. Fluids **26**, 1808 (1983).
[2] S. L. Cartier, N. D'Angelo, P. H. Krumm, and R. L. Merlino, Phys. Fluids **28**, 432 (1985).
[3] G. Ganguli, Y. C. Lee, and P. J. Palmadesso, Phys. Fluids **28**, 761 (1985); Phys. Fluids **31**, 823 (1988).
[4] G. Ganguli, Y. C. Lee, and P. J. Palmadesso, Phys. Fluids **31**, 2753 (1988).
[5] H. Romero and G. Ganguli, Phys. Fluids B **4**, 1708 (1992).
[6] A. N. Mostovych, B. H. Ripin, and J. A. Stamper, Phys. Rev. Lett. **62**, 2837 (1989).
[7] T. A. Peyser, C. K. Manka, B. H. Ripin, and G. Ganguli, Phys. Fluids B **4**, 2448 (1992).
[8] A. Matsubara and T. Tanikawa, Jpn. J. Appl. Phys. **39**, 4920 (2000).
[9] T. A. Santhosh Kumar, S. K. Matoo, and R. Jha, Phys. Plasmas **9**, 2946 (2002).
[10] W. E. Amatucci, G. Ganguli, D. N. Walker, G. Gatling, M. Balkey, and T. McCulloch, Phys. Plasmas **10**, 1963 (2003).
[11] G. Ganguli, M. J. Keskinen, H. Romero, R. Heelis, T. Moore, and C. Pollock, J. Geophys. Res. **99**, 8873 (1994).
[12] N. Rynn and N. D'Angelo, Rev. Sci. Instrum. **31**, 1326 (1960).
[13] W. E. Amatucci, J. Geophys. Res. **104**, 14481 (1999).
[14] K.-I. Nishikawa, G. Ganguli, Y. C. Lee, and P. J. Palmadesso, J. Geophys. Res. **95**, 1029 (1990).
[15] K.-I. Nishikawa, G. Ganguli, Y. C. Lee, and P. J. Palmadesso, Phys. Fluids **31**, 1568 (1988).
[16] P. L. Pritchett, Phys. Fluids B **5**, 3770 (1993).
[17] D. Cai, L. R. O. Storey, and T. Neubert, Phys. Fluids B **2**, 75 (1989).
[18] M. E. Koepke, J. J. Carroll III, and M. W. Zintl, Phys. Plasmas **5**, 1671 (1998).
[19] D. N. Hill, S. Fornaca, and M. G. Wickham, Rev. Sci. Instrum. **54**, 309 (1983).
[20] V. Laul, N. Rynn, and H. Bohmer, Rev. Sci. Instrum. **48**, 1499 (1977).
[21] P. J. Paris, Rev. Sci. Instrum. **60**, 2802 (1989).
[22] M. E. Koepke, M. W. Zintl, C. Teodorescu, E. W. Reynolds, G. Wang, and T. N. Good, Phys. Plasmas **9**, 3225 (2002).
[23] M. E. Koepke and W. E. Amatucci, IEEE Trans. Plasma Sci. **20**, 631 (1992).
[24] W. E. Drummond and M. N. Rosenbluth, Phys. Fluids **5**, 1507 (1962).
[25] R. W. Motley and N. D'Angelo, Phys. Fluids **6**, 296 (1963).
[26] P. H. Krumm and M. J. Alport, Plasma Phys. Controlled Fusion **26**, 1007 (1984); E. G. van Niekerk, P. H. Krumm, and M. J. Alport, Plasma Phys. Controlled Fusion **33**, 375 (1991).
[27] D. L. Correll, N. Rynn, and H. Bohmer, Phys. Fluids **18**, 1800 (1975).
[28] R. F. Kemp and J. M. Sellen, Rev. Sci. Instrum. **55**, 455 (1966).
[29] F. F. Chen, *Introduction to Plasma Physics and Controlled Fusion* (Plenum, New York, 1990).
[30] W. E. Amatucci, D. N. Walker, G. Ganguli, D. Duncan, J. Antoniades, J. H. Bowles, V. Gavrishchaka, and M. E. Koepke, J. Geophys. Res. **103**, 11711 (1998).
[31] V. Gavrishchaka, Ph.D. thesis, Department of Physics, West Virginia University, 1996.